



ISTITUTO NAZIONALE DI RICERCA METROLOGICA Repository Istituzionale

Forward scattering in two-beam laser interferometry

Original

Forward scattering in two-beam laser interferometry / Mana, G; Massa, E; Sasso, C. P.. - In: METROLOGIA. - ISSN 0026-1394. - 55:2(2018), pp. 222-228. [10.1088/1681-7575/aaac4d]

Availability:

This version is available at: 11696/58598 since: 2018-09-14T14:43:25Z

Publisher:

Published

DOI:10.1088/1681-7575/aaac4d

Terms of use:

This article is made available under terms and conditions as specified in the corresponding bibliographic description in the repository

Publisher copyright

(Article begins on next page)

PAPER • OPEN ACCESS

Forward scattering in two-beam laser interferometry

To cite this article: G Mana *et al* 2018 *Metrologia* **55** 222

View the [article online](#) for updates and enhancements.

Related content

- [Wavefront errors in a two-beam interferometer](#)
G Mana, E Massa and C P Sasso
- [Measurement of the lattice parameter of a silicon crystal](#)
E Massa, G Mana, U Kuetgens et al.
- [The self-weight deformation of an x-ray interferometer](#)
L Ferroglio, G Mana and E Massa

Recent citations

- [Wavefront errors in a two-beam interferometer](#)
G Mana *et al*

Forward scattering in two-beam laser interferometry

G Mana[✉], E Massa[✉] and C P Sasso[✉]

INRIM—Istituto Nazionale di Ricerca Metrologica, Str. delle Cacce 91, 10135 Torino, Italy

E-mail: g.mana@inrim.it

Received 29 September 2017, revised 26 January 2018

Accepted for publication 31 January 2018

Published 28 February 2018



Abstract

A fractional error as large as 25 pm mm^{-1} at the zero optical-path difference has been observed in an optical interferometer measuring the displacement of an x-ray interferometer used to determine the lattice parameter of silicon. Detailed investigations have brought to light that the error was caused by light forward-scattered from the beam feeding the interferometer. This paper reports on the impact of forward-scattered light on the accuracy of two-beam optical interferometry applied to length metrology, and supplies a model capable of explaining the observed error.

Keywords: interferometry, length metrology, diffraction, scattering

(Some figures may appear in colour only in the online journal)

1. Introduction

Laser interferometry is widely used in dimensional metrology. The ability to deliver high-bandwidth, low-noise, sensitive and accurate position and angle information allows interferometers to be used in precision measurements and feedback loops. Exemplar applications include measurements of the Planck [1] and Avogadro constants [2], free-fall gravimetry [3], γ -ray spectrometry [4], and the detection of gravitational waves [5]. All these measurements require state-of-the-art investigations of the interferometer operation as regards the impact of, among others, diffraction [6–8], wavefront stability and errors [9], beam alignment [10, 11], ghost, stray and recycled light [12], and polarization delivery [4, 13].

Combined optical and x-ray interferometry is a unique tool to investigate the performance of laser interferometry in high-resolution and high-accuracy measurements of spatial dimensions. Our experimental set-up is devoted to the measurement of the lattice parameter of silicon (Si) monocrystals to within a fractional accuracy approaching 1 pm mm^{-1} [14, 15].

In order to achieve such a small uncertainty, the operation of the optical interferometer was investigated from both experimental and theoretical viewpoints to identify any

phenomenon which could interfere with the measurement and to understand the underlying physics. In 2016, having completed the lattice parameter measurements and keeping in mind reductions of the noise induced by the frequency stabilization, we reassembled the optical interferometer to make the arm lengths equal. Doing this, we observed a measurement error as large as 25 pm mm^{-1} at the zero optical-length difference of the interferometer arms.

In this paper, after outlining the operation of a combined x-ray and optical interferometer, we report on the observations made. Next, we propose a model explaining the data in terms of the self-interference of forward-scattered light. On this basis, we observed that it is possible to reduce the impact of scattered light by reducing the detector aperture. Subsequent measurements of the lattice parameter confirmed the prediction and the effectiveness of this remedy.

2. X-ray/optical interferometry

As shown in figure 1, a combined x-ray and optical interferometer consists of three Si crystals (about 5 cm long and 1 mm thick) cut so that the (220) diffracting planes are orthogonal to the crystal surfaces. X-rays are split by the first two crystals and recombined by an analyser crystal. When the analyser is moved orthogonally to the (220) planes, a periodic variation of the transmitted and diffracted x-ray intensities is observed, the period being the diffracting-plane



Original content from this work may be used under the terms of the [Creative Commons Attribution 3.0 licence](https://creativecommons.org/licenses/by/3.0/). Any further distribution of this work must maintain attribution to the author(s) and the title of the work, journal citation and DOI.

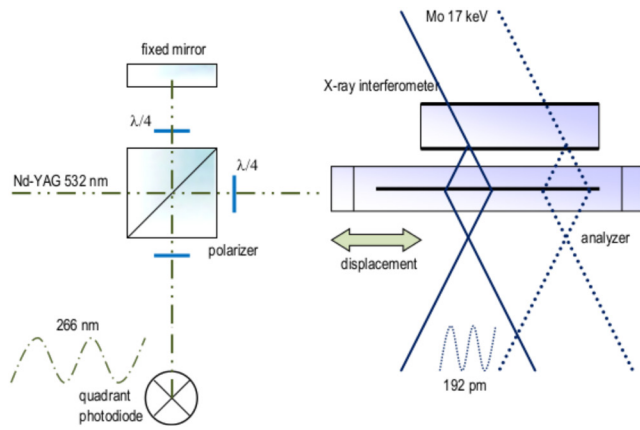


Figure 1. Top view of a combined x-ray and optical interferometer. The laser beam wavelength and divergence are 532 nm and 0.25 mrad, to which a $w_0 \approx 0.7$ mm waist radius and $z_R \approx 3$ m Rayleigh distance will correspond. The detector distance from the beam waist is about 1.5 m. The dotted lines indicate the displaced x-ray path used to check which ruler (crystal or optical) the dip is fastened to.

spacing. The analyser embeds a front mirror so that displacements up to 5 cm are measured by optical interferometry. The frequency of the laser source is locked to a transition of the $^{127}\text{I}_2$ molecule and the necessary picometer resolution is achieved by polarization encoding and phase modulation. To eliminate the adverse influence of the refractive index of air and temperature, the measurement is carried out in a vacuum chamber of about 0.6 m diameter and the temperature is controlled up to millikelvin stability and uniformity. Parasitic rotations and transverse motions are sensed via laser interferometry and a capacitive transducer; feedback loops provide picometer positioning, nanoradian alignment, and nanometer straightness.

3. Experimental tests

The measurement equation is $d = m\lambda/(2n)$, where d is the diffraction-plane spacing, and n is the number of x-ray fringes in m optical fringes of $\lambda/2$ period. In practice, the lattice spacing is determined by comparing the periods of the x-ray and optical fringes. This is done by measuring the x-ray fringe fraction at the ends of increasing displacements and updating the $\lambda/(2d)$ ratio at each step. The measurement resolution approaches 1 pm mm^{-1} , which means that the experiment is sensitive to $10^{-9}\lambda$ variations of the beam wavelength.

Figure 2 shows the fractional variations of the measured lattice-spacing values along a horizontal line 20 mm long, where the origin of the abscissa is the null difference of the path lengths of the laser beam through the interferometer. Each measurement was carried out over analyser displacements of 1 mm. In a small neighbourhood of the origin, the measured d values display a 25 pm mm^{-1} dip. Subsequent tests made by sliding the x rays (as shown in figure 1) confirmed that the dip is not due to a local strain of the analyser lattice, but it stays anchored to the zero-length difference of the interferometer arms. Therefore, the dip indicates a local variation of the effective wavelength of about $25 \times 10^{-9}\lambda$ having a full width at half maximum equal to 3.4 mm.

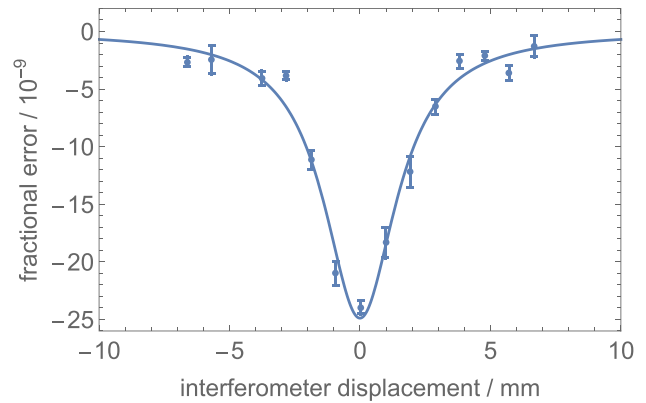


Figure 2. Fractional variations of the measured lattice-spacing values along a horizontal line 20 mm long. Each measurement averages a 1 mm crystal slice. The solid line is the Lorentzian function best fitting the data.

4. Interferometer model

The calibration of the laser frequency achieves relative uncertainties smaller than 10^{-10} , but it is not possible to calculate the effective wavelength, as obtained from the period of the integrated interference pattern, from the frequency via the plane-wave dispersion equation. Diffraction, wavefront stability and errors, beam quality, ghost, stray and recycled light, and polarization wandering can never be fully eliminated and must be reduced to acceptable levels or quantified and corrected.

To explain the dip of the measured d values, after many experimental tests and numerical simulations, we focused our attention on the scattered light. Within a heuristic approximation, forward-scattered light behaves like an additional (collinear and divergent) Gaussian beam feeding the interferometer and contributing to the effective wavelength proportionally to the scattered-light intensity. In the following, we study the period of the integrated signal of a two-beam interferometer fed by, firstly, a Gaussian beam, and secondly, a coherent superposition of Gaussian beams, one collimated and the others scattered from the first.

4.1. Gaussian beam

Let the interferometer be fed by the Gaussian beam

$$u_0(x, y) = e^{-(x^2 + y^2)/2}, \quad (1)$$

where we factored the $\exp(-ikz)$ term of the optical fields, k is the plane-wave wave number, z the propagation distance, the dimensionless coordinates x and y are measured in $w_0/\sqrt{2}$ units, and w_0 is the waist radius—which is equal to $\sqrt{2}$ when expressed in $w_0/\sqrt{2}$ units. At a $\zeta = z/z_R$ distance from the waist, the reciprocal space representation of the complex amplitude is

$$\tilde{u}_0(p, q; \zeta) = U(p, q; \zeta)\tilde{u}_0(p, q), \quad (2)$$

where $z_R = kw_0^2/2$ is the Rayleigh distance, the dimensionless impulses p and q are the variables conjugate to x and y ,

$$U(p, q; \zeta) = e^{i(p^2 + q^2)\zeta/2} \quad (3)$$

and

$$\tilde{u}_0(p, q) = e^{-(p^2+q^2)/2} \quad (4)$$

are the reciprocal space representations—having $e^{-i(px+qy)}$ basis functions—of the free-space paraxial propagator and (1), respectively.

We assume that the interferometer slides the interfering beams, $|u_0(z)\rangle$ and $|u_0(z+s)\rangle$, one with respect to the other while keeping them coaxial, and that the length difference s of the interferometer arms is the sliding distance. The phase of the integrated interference pattern in excess or defect with respect to the dynamical phase, $-ks$, is

$$\phi(\varsigma) = \arg[\Xi(\varsigma)] = \arctan(\varsigma/2), \quad (5)$$

where, by using the bra-ket notation for the inner product and the reciprocal space representations (3) and (4),

$$\begin{aligned} \Xi(\varsigma) &= \langle u_0 | U^\dagger(\varsigma) U(\varsigma + \varsigma) | u_0 \rangle \\ &= \int_{-\infty}^{+\infty} \int_{-\infty}^{+\infty} \tilde{u}_0(p, q) U(p, q; \varsigma) \tilde{u}_0(p, q) dp dq \\ &= \int_{-\infty}^{+\infty} \int_{-\infty}^{+\infty} e^{i(p^2+q^2)\varsigma/2} e^{-(p^2+q^2)} dp dq = \frac{2\pi}{2-i\varsigma}, \end{aligned} \quad (6)$$

is the autocorrelation of $|u_0(z)\rangle$, the \dagger superscript indicates the conjugate transpose, and $\varsigma = s/z_R$. It is worth noting that $U^\dagger(\varsigma)U(\varsigma + \varsigma) = U(\varsigma)$; therefore, (6) depends only on the length difference of the interferometer arms, not on the detection-plane distance from the beam waist.

The effective wavelength is

$$\lambda_e(\varsigma) = \lambda \left[1 + \frac{\partial_s \phi(s)}{k} \right] = \lambda \left[1 + \frac{\theta_0^2}{4(1+\varsigma^2/4)} \right], \quad (7)$$

where λ is the plane-wave wavelength and $\theta_0 = 2/(kw_0) = \sqrt{2/(kz_R)}$ is the beam divergence. The (positive) sign of the derivative in (7) is dictated by the (negative) sign chosen for the plane-wave propagation, i.e. in $\exp(-ikz)$. The fractional difference of the effective wavelength from the plane-wave one is

$$\frac{\Delta\lambda}{\lambda} = \frac{\theta_0^2}{4(1+\varsigma^2/4)}, \quad (8)$$

where $\Delta\lambda = \lambda_e - \lambda$. The $\theta_0^2/4$ term is the trace of the second central-moment of the angular spectrum, which is the standard ingredient to calculate the effective wavelength and takes the diffraction of arbitrary paraxial beams into account [6, 8]. An effective wavelength greater than the plane-wave wavelength means that, when calculating the wavelength from frequency by the $\lambda = c/\nu$ dispersion relation, optical interferometry underestimates the measurand.

As shown in figure 3, the $1/(1+\varsigma^2/4)$ factor acts as a bandpass filter and restricts the effect of diffraction to an interval of about $4z_R$ (full width at half maximum) centred on the equal-arm configuration of the interferometer. The typical divergence of the beams customarily used for dimensional measurements ranges from 0.1 mrad–1 mrad. By observing that $z_R = 2/(k\theta_0^2)$, the width of the $1/(1+\varsigma^2/4)$ Lorentzian function ranges from 80 m–0.8 m, respectively.

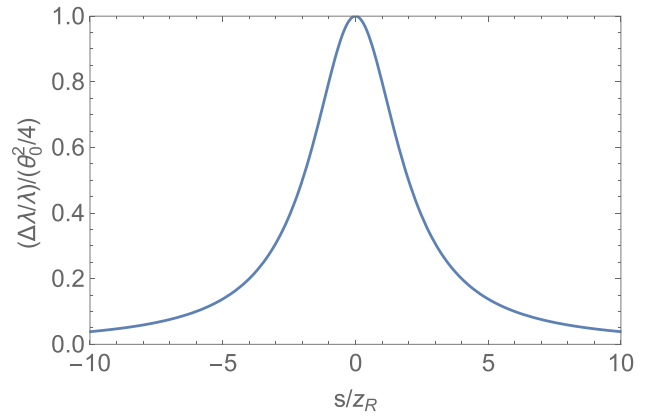


Figure 3. Gaussian beam. Normalized fractional variation of the effective wavelength. The abscissa is the optical path difference between the interferometer arms, normalized by the Rayleigh distance.

However, if the divergence is in the [10, 100] mrad interval, corresponding to waist radii in the [2, 20] μm interval, the Lorentzian's width is in the [0.08, 8] mm interval. Heuristically, if the effects superpose linearly, the light scattered by micro-metre size imperfections will explain the observed dip.

4.2. Forward scattering

Forward scatter is the diffraction by an absorption of refraction inhomogeneity having dimensions that are larger than λ , but much smaller than the beam diameter. The scattered light diverges but propagates in a direction collinear to the laser beam. Therefore, let the interferometer be illuminated by the superposition

$$u(x, y) = e^{-(x^2+y^2)/2} + ue^{i\alpha} e^{-[(x-x_0)^2+(y-y_0)^2]/(2a^2)} \quad (9)$$

where the second term is a wave diffracted by a scatterer located in (x_0, y_0) , the transverse coordinates are still measured in $w/\sqrt{2}$ units, w is the beam radius, $a \ll 1$ is the fractional radius of the scattering center, $a^2 u^2 \ll 1$ is the fractional scattered-power, $ue^{i\alpha}$ describes absorption as well refraction inhomogeneities, and the amplitude u is not constrained in size. In (9), we neglected the curvature of the Gaussian wavefront; therefore, the detector distance ς in (2) and (6) must be measured from the scatterer.

If (9) feeds the interferometer, by repeating the calculations in (6), where the Fourier transform of (9) substitutes for $\tilde{u}_0(p, q)$, the $|u(z)\rangle$ autocorrelation is

$$\Xi(\varsigma) = \frac{2\pi}{2-i\varsigma} + \frac{2\pi a^4 u^2}{2a^2-i\varsigma} + \frac{4\pi a^2 u \cos(\alpha) e^{-\frac{r_0^2}{2(1+a^2-i\varsigma)}}}{1+a^2-i\varsigma}, \quad (10)$$

where $r_0^2 = x_0^2 + y_0^2$. It must be noted that, when u or a tend to zero, this equation reproduces (6), as expected. The first term describes the self-interference of the Gaussian beam. The second describes the self-interference of the scattered wave. The last term describes the interferences of a Gaussian beam travelling along one interferometer arm with a scattered wave travelling along the other.

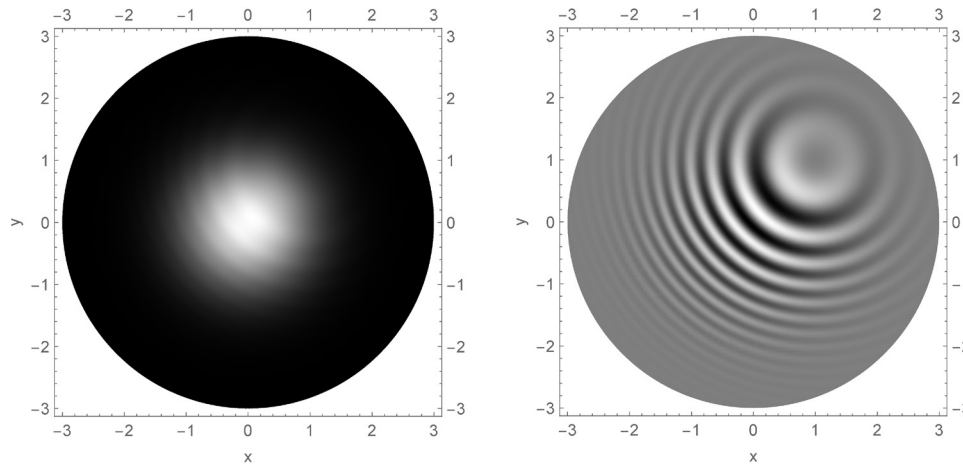


Figure 4. Left: interference pattern of a scatterer in $x_0 = y_0 = 1$ (dimensionless units) having fractional radius $a = 0.03$. The detection plane is at $\zeta = z/z_R = 0.1$ distance from the scatterer. Right: the Newton rings have been enhanced by subtracting the pattern due to the Gaussian beam and rescaling the image.

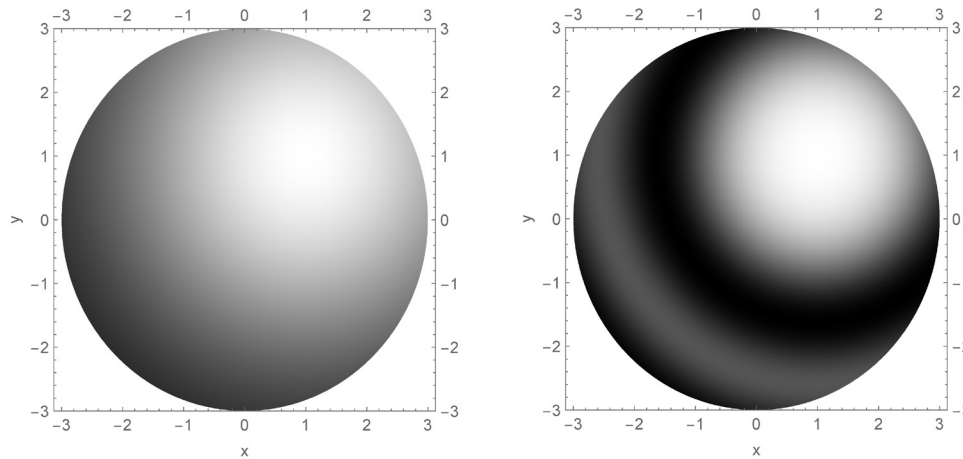


Figure 5. Interference pattern of a scatterer in $x_0 = y_0 = 1$ (dimensionless units) having fractional radius $a = 0.03$. The detection plane is at $\zeta = z/z_R = 0.1$ distance from the scatterer. With respect to figure 4, only the (rescaled) contribution due to the scattered wave has been shown. The length difference of the interferometer arms are zero (left) and $s/z_R = 0.01$ (right).

Figure 4 shows the interference pattern on the detection plane. The rings are due to the interference between the scattered and Gaussian waves travelling together along the same interferometer arm. Since they are static, they do not contribute to (10) and the fringe phase. The split and recombined scattered wave generates the rings shown in figure 5, which are superimposed onto those shown in figure 4, and, after integration over the detection plane, generate the second term in (10). Additional rings, not shown in figures 4 and 5, are associated with the last term of (10). They are due to the interference between the scattered and Gaussian waves travelling along different arms of the interferometer.

The effective wavelength can be calculated in the same way as in section 4.1. The result is a useless algebraic expression which is not given here. Figure 6 shows the normalized fractional variation of the effective wavelength in the neighbourhood of the null difference of the interferometer arms. It confirms that the dip shown in figure 2 originates from scattered light. The Rayleigh distance of the Gaussian beam illuminating the interferometer is about 3 m. Consequently, by fitting our

model to the data, we estimated that the effective amplitude of the scattered wave and scatterer size are $u \approx 0.7$ and $a \approx 0.03$, respectively. The fractional power of the beam feeding the interferometer that is scattered into the parasitic beam is 6×10^{-4} .

Numerical experiments indicated that the (x_0, y_0) coordinates, as well as the phase α , are irrelevant; the effective wavelength is affected only by the scattered power and the size of the scattering centre. The lowest order approximations,

$$\frac{\Delta\lambda}{\lambda} \approx \frac{\theta_0^2}{4} \left(1 + \frac{u^2}{1 + 3\zeta^2/(4a^4)} \right) \text{ if } \zeta/a^2 \ll 1, \quad (11a)$$

$$\frac{\Delta\lambda}{\lambda} \approx \frac{\theta_0^2}{4} \left(\frac{1}{1 + \zeta^2/4} \right) \text{ if } \zeta/a^2 \gg 1, \quad (11b)$$

confirm the numerical clues. They have been obtained by implementing (5) and (7) into a Mathematica [16] script. It is convenient to merge (11a) and (11b) into a single expression and to write the result in terms of the fractional power $I_1 = a^2 u^2$, divergence $\theta_1 = \theta_0/a$, and Rayleigh distance $z_{R1} = a^2 z_R$ of the scattered wave. Hence,

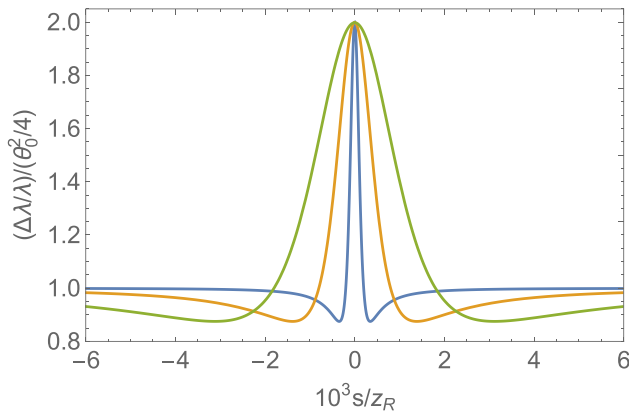


Figure 6. Forward scattering. Zoom of the normalized fractional variation of the effective wavelength when $u = 1$. The dimensionless sizes of the scatterer are above the plot. The abscissa is the optical path difference between the interferometer arms, normalized to the Rayleigh distance.

$$\frac{\Delta\lambda}{\lambda} \approx \frac{\theta_0^2}{4(1 + \varsigma^2/4)} + \frac{\theta_1^2 I_1}{4(1 + \varsigma_1^2/4)}, \quad (12)$$

where $\varsigma = s/z_R$ and $\varsigma_1 = \sqrt{3}\varsigma/a^2 = \sqrt{3}s/z_{R1}$. This equation shows that the scattered light contribution is added linearly, but scaled by the power and Rayleigh distance of the scattered wave.

The inspection of (10) shows that, for large $\varsigma = s/z_R$ values, the fringe phase in excess of $-ks$ originates from the Gaussian beam, while, for small $\varsigma = s/z_R$ values, it originates from the scattered waves. The contribution of the last term of (10)—which describes the interference between the Gaussian and scattered waves—is always overpowered by one of the other two. The curvature of the Gaussian wavefront would only have affected this term, thus justifying our decision to neglect it. The factor $\sqrt{3}$ in the ς_1 definition reflects the fact that the phase of the sum of the first two terms of (10), which are the only ones relevant to (12), is not the sum of their phases.

4.3. Multiple scattering

The results of section 4.2 can be extended to many scatterers. In this case, the light feeding the interferometer is

$$u(x, y) = e^{-(x^2 + y^2)/2} + \sum_n u_n e^{i\alpha_n} e^{-[(x - x_n)^2 + (y - y_n)^2]/(2a_n^2)}, \quad (13)$$

where the subscript n labels the scatterers. By repeating the calculations in (6) again, where the Fourier transform of (13) substitutes for $\tilde{u}_0(p, q)$, the $|u(z)\rangle$ autocorrelation is

$$\begin{aligned} \Xi(\varsigma) = & \frac{2\pi}{2 - i\varsigma} + \sum_n \frac{2\pi a_n^4 u_n^2}{2a_n^2 - i\varsigma} + \sum_n \frac{4\pi a_n^2 u_n \cos(\alpha_n) e^{-\frac{r_n^2}{2(1 + a_n^2 - i\varsigma)}}}{1 + a_n^2 - i\varsigma} \\ & + \sum_{m > n} \frac{4\pi a_m^2 a_n^2 u_m u_n \cos(\alpha_m - \alpha_n) e^{-\frac{r_{mn}^2}{2(a_m^2 + a_n^2 - i\varsigma)}}}{a_m^2 + a_n^2 - i\varsigma}, \end{aligned} \quad (14)$$

where $r_n^2 = x_n^2 + y_n^2$ and $r_{mn}^2 = (x_m - x_n)^2 + (y_m - y_n)^2$. The last term of (14) takes the interference between the light

scattered by different scatterers and travelling along different interferometer arms into account. Unless $r_{mn} \approx 0$, in which case we have a single scattering centre, it is irrelevant. Therefore, remembering the analysis in section 4.2, (14) can be approximated by

$$\Xi(\varsigma) \approx \frac{2\pi}{2 - i\varsigma} + \sum_n \frac{2\pi a_n^4 u_n^2}{2a_n^2 - i\varsigma}. \quad (15)$$

Also in this case, the lowest order approximation of the fractional variation of the effective wavelength,

$$\frac{\Delta\lambda}{\lambda} \approx \frac{\theta_0^2}{4(1 + \varsigma^2/4)} + \sum_n \frac{\theta_n^2 I_n}{4(1 + \varsigma_n^2/4)}, \quad (16)$$

was obtained by implementing (5) and (7) into a Mathematica [16] script. In (16), $I_n = a_n^2 u_n^2$ is the n th fractional power, $\theta_n = \theta_0/a_n$ is the n th divergence, $z_{Rn} = a_n^2/z_R$ is the n th Rayleigh distance, and $\varsigma_n = \sqrt{3}\varsigma/a_n^2 = \sqrt{3}s/z_{Rn}$.

4.4. Finite area detector

One way to limit the adverse effect of the scattered light is to limit the detection area so that the diffraction rings lie outside the detector. Therefore, in this section, we calculate the effective wavelength when the interference pattern is integrated over a finite-area detector.

4.4.1. Gaussian beam. To take the detector area into account, the interfering beams are projected in a disk centered on the beam axis, having

$$\rho(\zeta_1, \zeta_2) = \frac{\sqrt{1 + \zeta_1^2} + \sqrt{1 + \zeta_2^2}}{\sqrt{2}} \rho_0 \quad (17)$$

dimensionless radius, where ζ_1 and ζ_2 are the detector distances from the waists of the interfering Gaussian beams. This choice ensures that the ratio ρ_0 between the detector radius and the mean radius of the interfering beams is a constant. Hence,

$$\Xi(\zeta_1, \zeta_2) = \langle u_0 | U^\dagger(\zeta_2) \Pi(\rho) U(\zeta_1) | u_0 \rangle = \frac{2\pi \left(1 - e^{-\frac{\rho^2(2 - i\varsigma)}{2(\zeta_2 + i)(\zeta_1 - i)}} \right)}{2 - i\varsigma}, \quad (18)$$

where we used the direct-space representation of $U(\zeta)|u_0\rangle$, $\varsigma = \zeta_2 - \zeta_1$, and $\Pi(\rho; r) = 1$ if $r < \rho$ and $\Pi(\rho; r) = 0$ if $r > \rho$. It must be noted that (18), contrary to (6), depends separately on the lengths, ζ_1 and ζ_2 , of the interferometer arms. The effective wavelength,

$$\lambda_e(\zeta_1, \varsigma) = \lambda \left[1 + \frac{\partial_\varsigma \arg[\Xi(\zeta_1, \zeta_1 + \varsigma)]}{kz_R} \right], \quad (19)$$

where $\varsigma = s/z_R$ is the difference in the arm lengths, has been numerically calculated according to (7) from $\phi(\zeta_1, \zeta_2) = \arg \Xi(\zeta_1, \zeta_2)$. Figure 7 shows the normalized fractional variation $(\Delta\lambda/\lambda)/(\theta_0^2/4)$ when the interference pattern is integrated over detectors having dimensionless radius ρ_0 equal to infinity, 1.0, and 0.5.

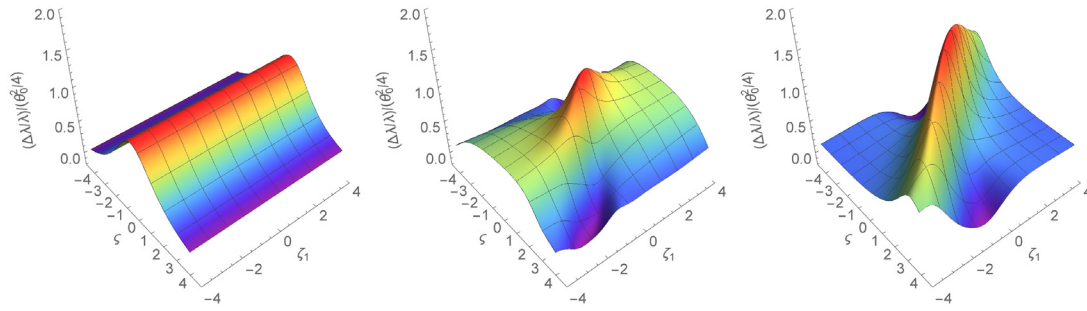


Figure 7. Gaussian beam and finite-area detector. Normalized fractional variation of the effective wavelength. The dimensionless detector-radii ρ_0 are infinity (left), 1.0 (center), and 0.5 (right).

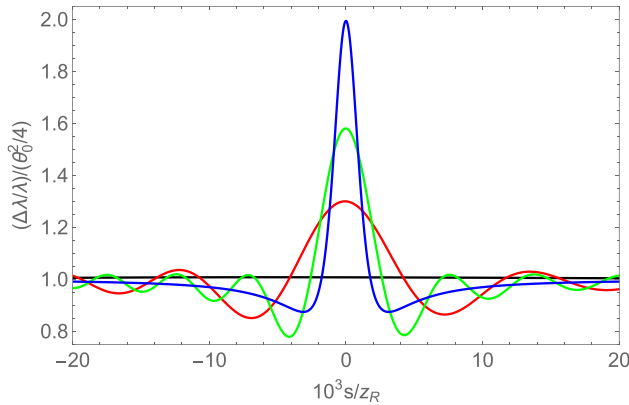


Figure 8. Forward scattering. Zoom of the normalized fractional variation of the effective wavelength when $u = 1$. The fractional size of the scatterer is $a = 0.03$, the detector-to-scatterer distance is $z = 0.2z_R$, the fractional detector-radii are indicated above the plot. The abscissa is the optical path difference between the interferometer arms, normalized to the Rayleigh distance.

4.4.2. Forward scattering. When the interferometer is illuminated by the superposition (9), in order to carry out a symbolic analysis as far as possible, we considered a scatterer located on the beam axis. Recalculating (18) and neglecting the contribution of the interference between the Gaussian and scattered beams, the $|u(z)\rangle$ autocorrelation is

$$\Xi(\zeta_1, \zeta_2) \approx \frac{2\pi \left(1 - e^{-\frac{\rho^2(2-i\zeta)}{2(\zeta_2+i)(\zeta_1-i)}} \right)}{2 - i\zeta} + \frac{2\pi a^4 u^2 \left(1 - e^{-\frac{\rho^2(2a^2-i\zeta)}{2(a^4+\zeta_1\zeta_2-ia^2\zeta)}} \right)}{2a^2 - i\zeta}, \quad (20)$$

where $\zeta = \zeta_2 - \zeta_1$. The dependence on the propagation distances ζ_1 and ζ_2 along the interferometer arms raises an important issue. In the first term, ζ_1 and ζ_2 are measured from the beam waist, while in the second term, they are measured from the scatterer.

The effective wavelength was obtained by numerically calculating the phase of (20) and its derivative with respect to the optical path difference $s = \zeta z_R$. The result is shown in figure 8. As heuristically expected, reducing the detection size washes out the peak at $\zeta = 0$; the oscillations are

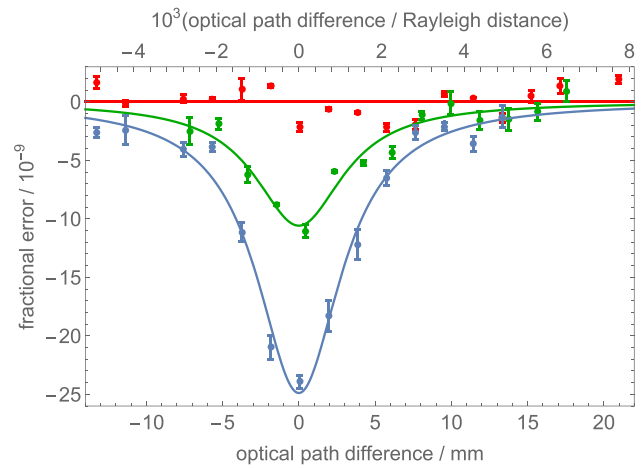


Figure 9. Fractional variations of the measured lattice-spacing value along a horizontal line 20 mm long (the optical path difference is two times the interferometer displacement). Blue: 6 mm detector radius. Green: 4 mm detector radius. Red: 2 mm detector radius. The solid lines are the Lorentzian functions best fitting the data.

due to the Newton ring crossing the detector edge. When the detector radius is about two times the beam size, or less, the peak disappears.

5. Conclusions

We have shown that, in optical interferometry applied to length metrology, the light scattered from the beam feeding the interferometer impacts significantly on the measurement accuracy. The proposed model of the interferometer operation explains the observation of a sharp dip of the measured interferometer-displacement centred on an equal-arm configuration by the self-interference of the scattered light travelling through the interferometer.

Our model suggests that a limited detector area significantly reduces the impact of the scattered-light. This prediction was experimentally confirmed by placing a variable iris in front of the detector and by repeating the measurements with different apertures. The results shown in figure 9 prove that we captured the essential aspects of the phenomenon.




Provided that the interferometer arms have different lengths, the forward scattering does not generate any errors. Since the measurements of the Si lattice parameter were carried

out—although without being aware of the benefit—with interferometer arms having sufficiently different lengths, the forward scattering did not affect the results given in [14, 15].

Appendix. List of the main symbols

w_0	waist radius
$z_R = kw_0/2$	Rayleigh distance
$\theta_0 = 2/(kw_0)$	beam divergence
$\zeta = s/z_R$	dimensionless propagation distance
$\varsigma = s/z_R$	dimensionless optical-path difference
$\Xi(\varsigma)$	autocorrelation of the beam complex-amplitude, equation (6)
λ_e	interference-fringe period, equation (7)
u, u_n	fractional amplitudes of the scattered waves
α, α_n	relative phases of the scattered waves
a, a_n	dimensionless radii of the scatterers
$I_n = a_n^2 u_n^2$	fractional powers of the scattered waves
$\theta_n = \theta_0/a_n$	divergence of the n th scattered wave
ρ_0	dimensionless detector radius, equation (17)

ORCID iDs

G Mana  <https://orcid.org/0000-0002-4109-7254>
 E Massa  <https://orcid.org/0000-0002-7764-3106>
 C P Sasso  <https://orcid.org/0000-0002-5715-7688>

References

- [1] Bielsa F, Robertsson L, Lavergne T, Kiss A, Fang H and Stock M 2016 *Conf. on Precision Electromagnetic Measurements* pp 1–2
- [2] Azuma Y *et al* 2015 *Metrologia* **52** 360–75
- [3] Zhang Z, Cheng Z, Qin Z and Zhu J 2007 *Chin. Opt. Lett.* **5** 344–6
- [4] Massa E, Mana G, Krempel J and Jentschel M 2013 *Opt. Express* **21** 27119–26
- [5] Pitkin M, Reid S, Rowan S and Hough J 2011 *Living Rev. Relativ.* **14** 5–75
- [6] Bergamin A, Cavagnero G, Cordiali L and Mana G 1999 *Eur. Phys. J. D* **5** 433–40
- [7] Andreas B, Ferroglio L, Fujii K, Kuramoto N and Mana G 2011 *Metrologia* **48** S104
- [8] Mana G, Massa E and Sasso C 2017 *Metrologia* **54** 559–65
- [9] Bender P L 2005 *Class. Quantum Grav.* **22** S339
- [10] Cavagnero G, Mana G and Massa E 2006 *J. Opt. Soc. Am. A* **23** 1951–9
- [11] Fujimoto H, Mana G and Nakayama K 2007 *IEEE Trans. Instrum. Meas.* **56** 351–5
- [12] Cavagnero G, Mana G and Massa E 2005 *Rev. Sci. Instrum.* **76** 053106
- [13] Bergamin A, Cavagnero G and Mana G 1992 *J. Mod. Opt.* **39** 2053–74
- [14] Massa E, Mana G, Kuetgens U and Ferroglio L 2011 *Metrologia* **48** S37
- [15] Massa E, Sasso C P, Mana G and Palmisano C 2015 *J. Phys. Chem. Ref. Data* **44** 031208
- [16] Wolfram Research Inc. 2017 Mathematica Version 11.2 (Champaign, IL: Wolfram Research Inc.)